Application of Attosecond Techniques to Condensed Matter Systems

DISSERTATION

Presented in Partial Fulfillment of the Requirements for the Degree Doctor of Philosophy in the Graduate School of The Ohio State University

By

Gregory J. Smith, M.Sc.

Graduate Program in Physics

The Ohio State University

2019

Dissertation Committee:

Louis F. DiMauro, Advisor

L. Robert Baker

Jay A. Gupta

Yuri V. Kovchegov

Table of Contents

List of Figures

Chapter 1

CONDENSED MATTER XUV
TRANSIENT ABSORPTION
EXPERIMENTS

1.1 Statement of Contribution

This experiment uses home-made equipment consisting of a XUV-IR Mach-Zhender inter-
ferometer, a bright XUV light source, a target chamber and an XUV photon spectrometer.
The entire apparatus was designed, built and tested by Gregory Smith and Stephen Hage-
man. The LabView software controlling the spectrometer's detector was programmed by
Kent Talbert. The vacuum system's safety system was designed and programmed by An-
drew Piper. The germanium samples were grown by Dr. Yaguo Tang. Transient absorption
experiments were done by Gregory Smith and Stephen Hageman. Analysis presented in this
document was done by Gregory Smith. Further details on the apparatus and the relevant
physics will be discussed in the main dissertation.

1.2 Introduction

We generate extreme ultraviolet (XUV) light using an extremely non-linear process called
high harmonic generation (HHG). Briefly, the XUV light source can be thought of as a
frequency comb spanning from ~ 20 eV to ~ 50 eV. The separation between the teeth of
the frequency comb is ω, the frequency of our laser light. In the time domain, the XUV
is a train of attosecond bursts of broadband light with an envelope of ~ 50 fs. Due to the
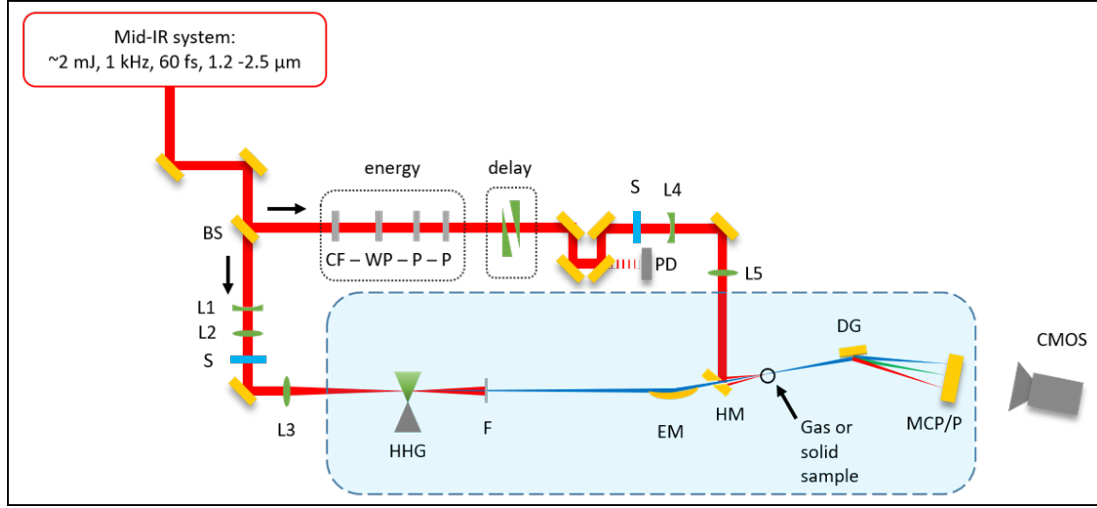
Figure 1.1: Schematic of the Transient Absorption BeamLine (TABLe). Blue shaded region is under vacuum. BS: beam splitter, L: lens, S: computer-controlled shutter, HHG: high harmonic generation, F: metallic filter, EM: ellipsoidal mirror, HM: hole mirror, PD: photodiode, DG: dispersive grating, MCP/P: micro-channel plate and phosphor.
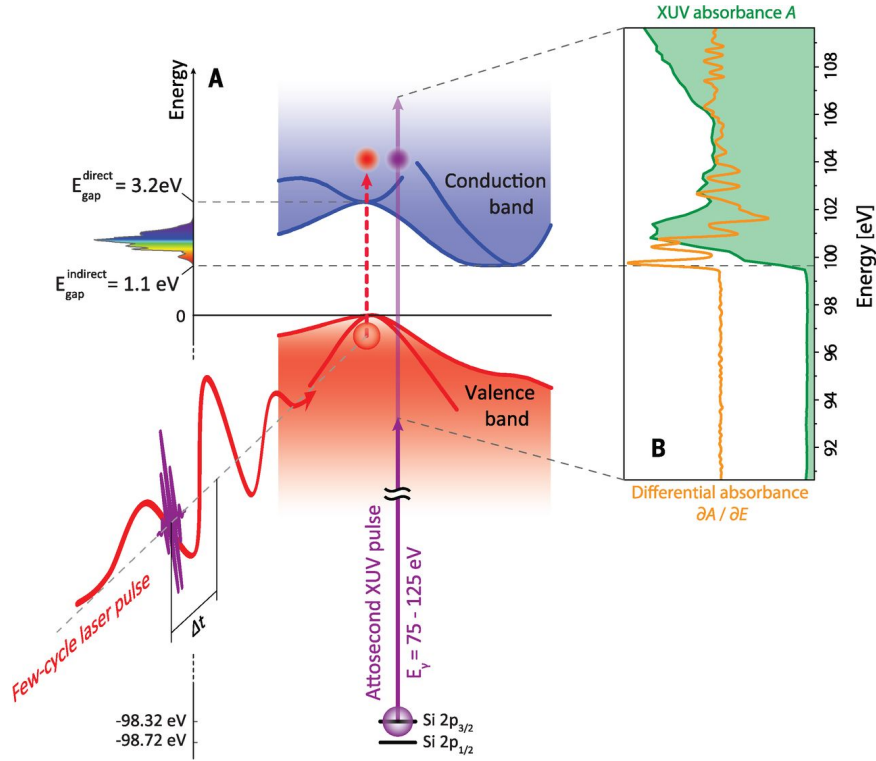
Figure 1.2: Schematic of an attosecond transient absorption spectroscopy (ATAS) experiment. An IR laser pulse excites electrons in the material, driving them across the band-gap. An XUV pulse passes through the sample after a delay Δt. The measured XUV absorbance is sensitive to electronic populations and states. Figure taken from [7].

ionizing nature of XUV light, the entire experiment must be performed under vacuum.

The experiment is powered by a commercial mid-IR laser system (Spectra Physics Spitfire ACE, Light Conversion HE TOPAS Prime), which delivers ~ 2 mJ at $100 - 1,000$ Hz repetition rate, ~ 65 fs duration, $1.2 - 2.5$ μm wavelength. The output of the TOPAS is routed into a Mach-Zhender interferometer, shown in Fig. 1.1. A beam splitter (BS) delivers the bulk of the pulse energy (96%) to the generation arm of the interferometer, which contains the HHG source and specialized XUV focusing optics. A small percentage of TOPAS's pulse energy goes to the pump arm, which contains optics to control the pulse energy and relative delay between the two arms. The pump arm also contains a series of lenses that focus the light into the vacuum system. A silvered hole mirror (HM) combines the two arms of the interferometer collinearly. This optic is designed to allow the XUV light to pass through a clear aperture on the backside of the HM while the pump arm's IR light reflects off the front face. The interferometer is aligned so that both arms have a common focus in the target chamber.

The basic concept of an attosecond transient absorption spectroscopy (ATAS) experiment is shown in Fig. 1.2. In this experiment, a sample is placed at the combined XUV/IR focus in a transmission (normal) geometry. An XUV photon spectrometer is placed behind the sample and the transmitted XUV spectrum S is measured as a function of XUV-IR delay. The IR light is not measured by the spectrometer.

Absorption features in the spectrum correspond to photoabsorption, which drive electronic transitions. At XUV photon energies, these transitions are from a core-level state to a state near the Fermi level. Since the HHG process produces a near-continuum, the XUV light will drive nearly all allowed transitions within its bandwidth. One of the core assumptions of an ATAS experiment is that the initial core state is shielded from the IR pulse by the valence electrons. However, the valence states are influenced by the external IR field, which causes both a change in electron population among these states, as well as a change in the states themselves. By measuring the XUV spectrum as a function of XUV-IR delay, we can track these electronic transitions - and thus the sample's electron dynamics - in response to an ultrafast optical excitation.
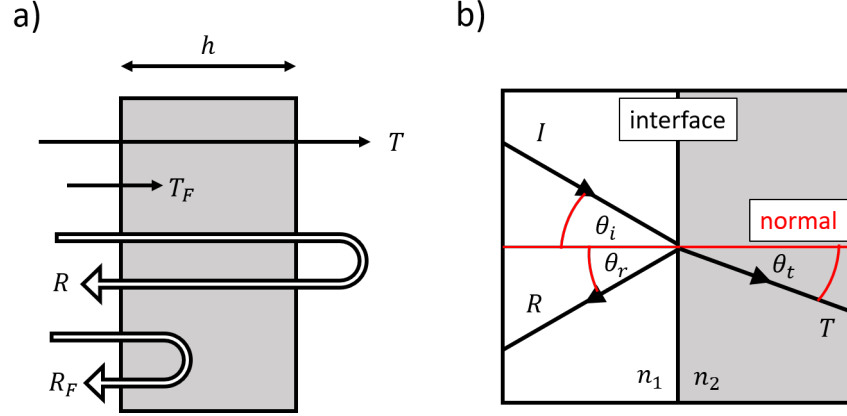
Figure 1.3: Normal and non-normal incident geometries. **a)** Normal incidence geometry showing Fresnel coefficients R_F, T_F for interfaces and total transmission T and reflectance R for a slab of thickness h. Figure recreated from [6]. **b)** Non-normal geometry showing definitions of angles θ_i, θ_r and θ_t with respect to each interface.

one way to think about ATAS: using the material's own electrons to probe their dynamics. i.e., the core electons are an electron source and they probe the dynamics near the Fermi level.

something, something physical motivation. maybe talk about what other measurements have done.

IR=pump, XUV=probe is not strictly true ... but it is a good approximation in solids.

need citations for this discussion, also maybe some equations.

excitation fraction of sample due to IR pump

estimation of ATAS transient absorption signal strength, based on XUV flux, excitation amount, etc.

1.2.1 Relative Contributions of Real and Imaginary Parts of $\tilde{n}$

In a transient absorption experiment, we measure the transmission T. Generally speaking, T depends on both parts of the complex refractive index: $\tilde{n} = n + ik$. However, in a normal transmission geometry it turns out that the contribution of $\text{Im}(\tilde{n})$ dominates the measured signal, and to a good approximation the role of $\text{Re}(\tilde{n})$ can be ignored. Note that
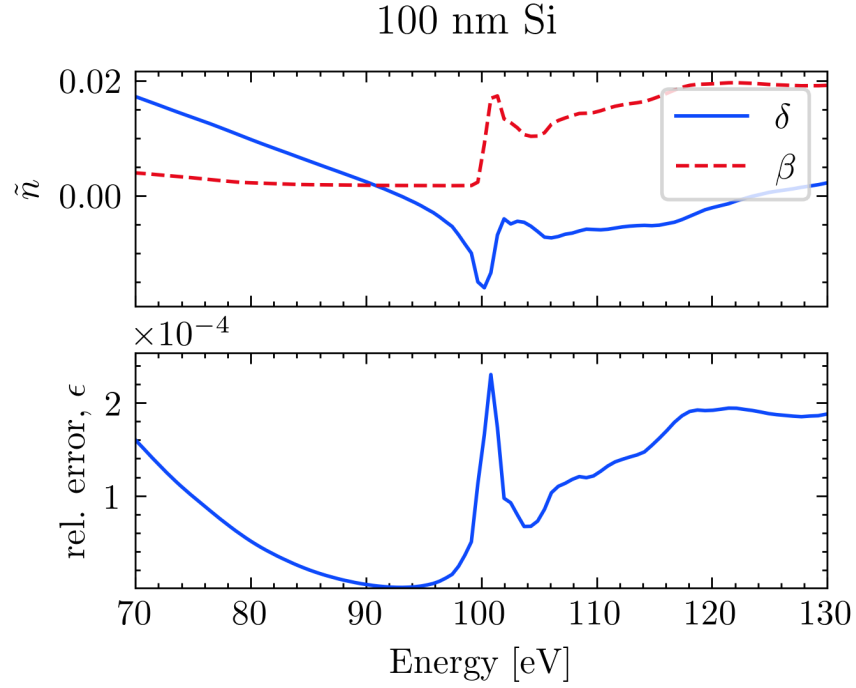
Figure 1.4: Consequences of ignoring the real part of $\tilde{n}$ when calculating the transmission T of a thin sample. Top panel: complex refractive index of silicon using the notation from Eq. (1.1). The Si L-edge absorption feature is visible near 100 eV. Data from [4]. Bottom panel: relative error in T, as defined in Eq. (1.8), introduced by ignoring the contribution of Re($\tilde{n}$). An infinite number of bounces (e.g., Eq. (1.6)) is assumed.

in a non-normal reflection geometry, both parts of $\tilde{n}$ make significant contributitions to the measured signal. In the following discussion we will analyze the Fresnel equations to see why this is the case. This section will draw from arguments made in reference [6].

First, we consider the normal geometry shown in the left panel of Fig. 1.3. We write the complex index of refraction in the following form:

$$\tilde{n} = n - ik$$
$$= (1 - \delta) - i\beta$$

(1.1)

The Fresnel coefficients R_F and T_F describe the interface reflectance and transmittance and depend on both parts of the complex index $\tilde{n}$. For normal incidence, they are:

$$R_F = \left| \frac{n - ik - 1}{n - ik + 1} \right|^2$$
$$T_F = \frac{4n}{|n - ik + 1|^2}$$

(1.2)

Absorption in the bulk is described via the absorption length α:

$$\alpha = 4\pi k / \lambda$$

(1.3)

Ignoring interface effects, the transmisison through the bulk is:

$$T_{\text{bulk}} = \exp(-\alpha h)$$

(1.4)

Note that α and T_{bulk} only depend on k.

The total reflectance R and transmission T are the result of interface effects plus bulk effects. Neglecting interference, we consider the case of N bounces where the laser's coherence length is less than the thickness of the bulk. In this case, the sum is incoherent with the expressions for T and R given by:

$$R = R_F + R_F T_F^2 T_{\text{bulk}}^2 \sum_{m=0}^{N} [R_F T_{\text{bulk}}]^{2m}$$
$$T = T_F^2 T_{\text{bulk}} \sum_{m=0}^{N} [R_F T_{\text{bulk}}]^{2m}$$

(1.5)

For the case of an infinite number of bounces, Eq. (1.5) simplifies to:

$$R = R_F + \frac{R_F T_F^2 T_{\text{bulk}}^2}{1 - R_F^2 T_{\text{bulk}}^2}$$

$$T = \frac{T_F^2 T_{\text{bulk}}^2}{1 - R_F^2 T_{\text{bulk}}^2},$$

(1.6)

whereas if only a single bounce occurs, Eq. (1.5) reduces to:

$$R = R_F + R_F T_F^2 T_{\text{bulk}}^2$$

$$T = T_F^2 T_{\text{bulk}}^2$$

(1.7)

We now consider the fractional error introduced by ignoring the interface effects described by T_F and R_F. That is, what would happen if we assume that the interfaces have no effect on the transmitted intensity? We introduce the relative error ϵ made by ignoring the Fresnel coefficients of Eq. (1.6):

$$\epsilon \equiv \frac{T_{\text{bulk}}}{T} - 1$$

(1.8)

As an example, consider a 100 nm thick Si sample measured in transmission near the Si L-edge (about 100 eV), as shown in Fig. 1.4. The relative error is in the range of one part in 10^4 to 10^5, well below our experimental detection limit. Silicon was chosen due to its data availability above and below the absorption edge, but this behavior is true for all materials in normal transmission.

The real part of the complex index becomes important when the sample isn't normal to the beam, as shown in the right panel of Fig. 1.3. In this case, the Fresnel equations are a bit messier:

$$R_s = \left| \frac{\tilde{n}_1 \cos \theta_i - \tilde{n}_2 \cos \theta_t}{\tilde{n}_1 \cos \theta_i + \tilde{n}_2 \cos \theta_t} \right|^2$$

$$R_p = \left| \frac{\tilde{n}_1 \cos \theta_t - \tilde{n}_2 \cos \theta_i}{\tilde{n}_1 \cos \theta_t + \tilde{n}_2 \cos \theta_i} \right|^2$$

$$T_s = 1 - R_s$$

$$T_p = 1 - R_p$$

(1.9)

Here, the subscripts s and p denote the polarization relative to the surface normal. In a vacuum, $\tilde{n}_1 = 1$ and $\tilde{n}_2$ is the index of the sample. We can extract the relevant physics

7
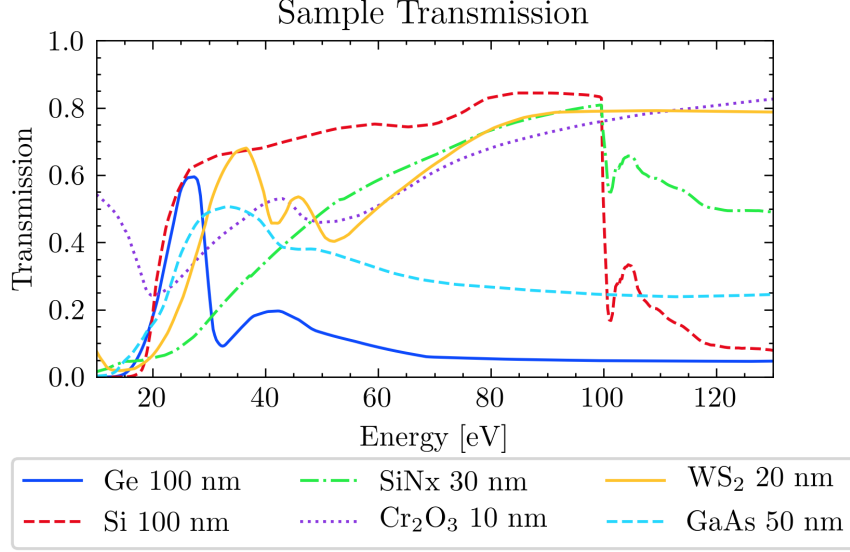
Figure 1.5: Calculated XUV transmission of various materials. Data from [4].

without any additional manipulation of the Eq. (1.9). Right away, we can see that unlike Eq. (1.2), Eq. (1.9) is symmetric in the real and imaginary parts of the sample's complex index, $\tilde{n}_2$. In the limit of a thick slab, $(h \gg \alpha)$, the light is attenuated before it can reflect off the back surface and we have $T \to 0$ and $R \to R_{s,p}$. That is, the only contributions to the reflected intensity are from the interface and possibly the sample volume within $z \approx 1/\alpha$ of the interface. As a result, both parts of $\tilde{n}_2$ will make significant contributions to the reflected intensity.

1.3 Sample Requirements and Geometry

There are several sample requirements for a successful condensed matter transient absorption experiment. First and foremost, the sample needs to have an absorption edge within the bandwidth of the XUV source. Second, the material must be the correct thickness for a transmission measurement, given the signal to noise of the appratus. If the material is too thick, the ground state will absorb most of the XUV flux and the resulting spectrum will be too close to the noise floor of the apparatus. If it is too thin, the laser-induced change of the ground state (on the order of $1 - 10\%$) will be lost in the noise. As a general guideline,
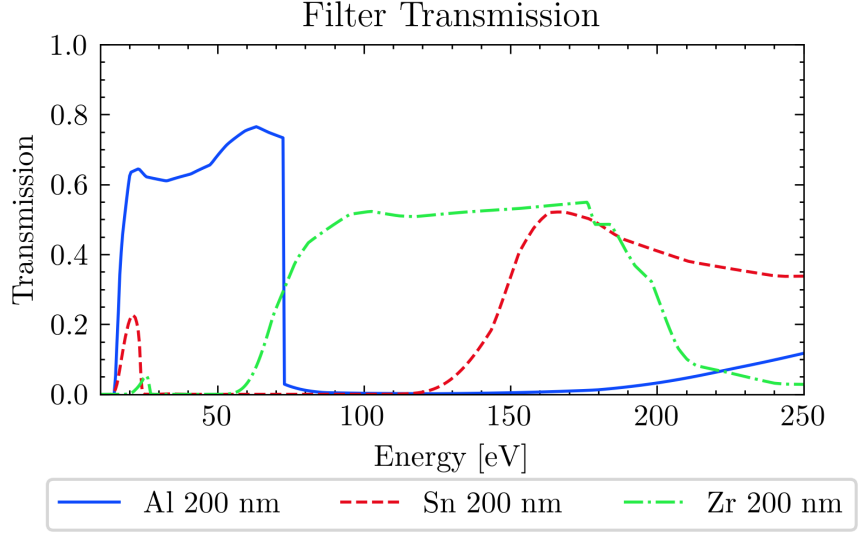
Figure 1.6: Calculated XUV transmission of various metallic filters. Data from [4].

a sample that absorbs 50% at the spectral feature of interest provides a good compromise between these conflicting requirements. Fig. 1.5 plots the expected transmission of several materials, calculated from the atomic scattering factors [4]. A typical sample will be on the order of 10 - 200 nm thick, depending on the material.

Next, the sample needs to be excitable using laser sources present in our lab (i.e., ultrafast pulses with wavelengths between 800 nm and a couple of microns). To minimize the slow build up of heat (on the order of seconds) and laser-induced damage, the sample needs to be rastered through the laser focus as the experiment is performed. This rastering method necessitates both a large clear aperture ($\sim$ 1 mm^2 - 1 cm^2) and good sample uniformity. Samples that meet the above thickness and clear aperture requirements are extremely delicate, with thicknesses between 5,000 and 100,000 times smaller than their freestanding lateral dimensions. As such, one should expect most samples to break before, during and after measurements, and a successful experiment will have a materials pipeline that is capable of producing multiple, consistent samples in a short time frame.

9
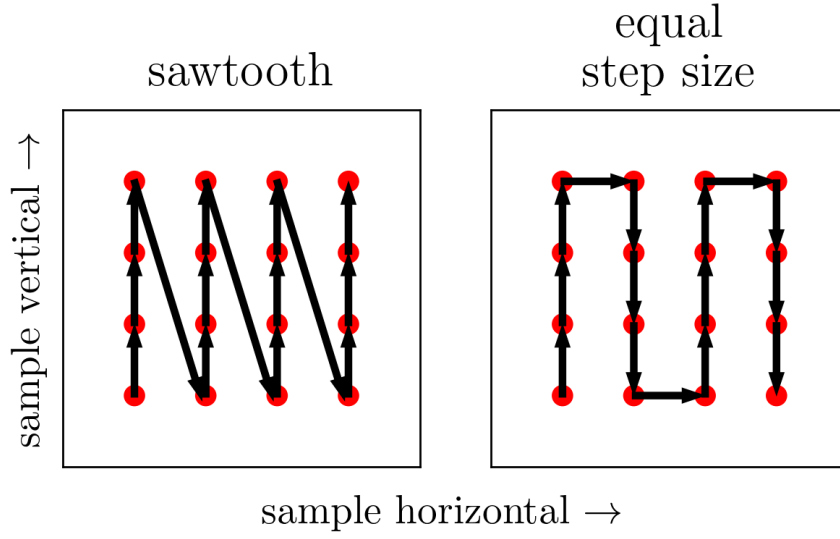
Figure 1.7: Schematic of competing raster methods, shown in the sample's reference frame. The clear aperture of the sample is represented by the interior of the black square. The laser propagation direction is out of the page. The laser focal spots are shown as red circles, and the movement of the sample holder relative to the laser focus is indicated by arrows. This diagram is to scale for a 1×1 mm^2 clear aperture sample, a 60 μm diameter IR focal spot and a 200 μm step size.
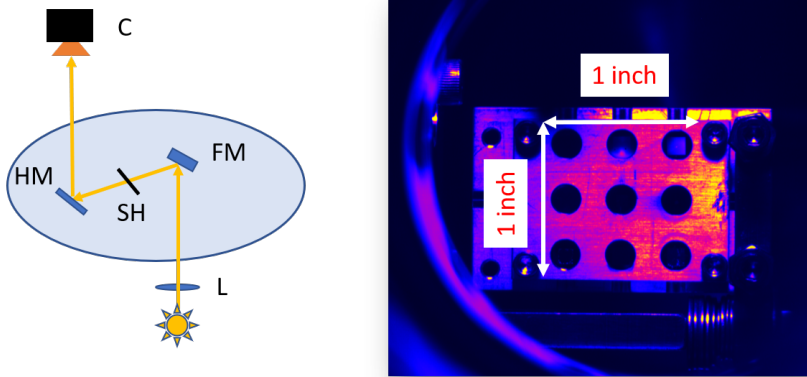
Figure 1.8: *In-situ* imaging of the samples within the target chamber. Left: optical setup for *in-situ* imaging of samples. C: Si CCD camera, HM: hole mirror, SH: sample holder, FM: flip mirror, L: lens. Right: false color image showing the sample holder with a 3 x 3 grid of 5 mm diameter clear apertures. Samples are held in a clamshell design centered in the clear apertures. Samples are backlit using a flashlight.

1.4 Data Collection

talk about general data collection here. i.e., what do you actually record during an experiment?

The absorbance[1] A is defined as the negative logarithm of the transmission:

$$A(E) = -\log_{10}(T) = -\log_{10}\left(\frac{S_{gs}(E)}{S_{vac}(E)}\right). \tag{1.10}$$

In Eq. (1.10), $S_{gs}(E)$ is the XUV spectrum transmitted by the sample in its ground state and $S_{vac}(E)$ is the spectrum without the sample present. Therefore we can measure the sample's ground state absorbance by measuring the harmonic spectrum with and without the sample in the XUV beam.

The *change in absorbance* ΔA between the ground and excited state which is induced by an IR pulse is therefore:

$$\begin{aligned}
\Delta A(E,\tau) &= A_{sig}(E,\tau) - A_{gs}(E) \\
&= -\log_{10}\left(\frac{S_{sig}(E,\tau)}{S_{vac}(E)}\right) - \log_{10}\left(\frac{S_{gs}(E)}{S_{vac}(E)}\right) \\
&= -\log_{10}\left(\frac{S_{sig}(E,\tau)}{S_{gs}(E)}\right).
\end{aligned} \tag{1.11}$$

In Eq. (1.11), the signal spectrum $S_{sig}(E,\tau)$ is the spectra that results from an IR pulse hitting the sample, followed by an XUV pulse after a delay of $\tau \equiv t_{XUV} - t_{IR}$. Note that negative delays mean the XUV arrives at the sample before the IR and zero delay indicates temporal overlap of the two pulses. It is assumed that a delay of negative infinity is equivalent to a ground state measurement: $S_{sig}(E, \tau = -\infty) = S_{gs}$.

An ATAS experiment is simply a collection of recorded spectra taken over a range of delay points with otherwise identical experimental conditions. However, we have implemented several techniques to improve the fidelity of our data.

HHG is an extremely inefficient process, with a conversion ratio on the order of 10^{-6}. After the generation cell, the leftover IR light must be blocked or it will destroy any sample located downstream. We use a thin metallic filter (Al, Zr or Sn), placed about 1 m after the

---

[1]The terms absorbance and optical density are often used interchangably.

harmonic source, to strip out the generating infrared field. The choice of filter is dictated by the features we want to study. For more detail, see Fig. 1.6.

As an extremely nonlinear process, HHG's conversion efficiency is highly dependent on the input laser pointing, peak power, pulse duration, spatial mode, etc. – all of which are affected by laboratory environmental conditions and the activity of other group members within our lab complex. As a result, the total harmonic yield drifts slowly throughout the course of the experiment. To minimize the effect of this slow drift, we take a ground state spectrum for each delay point. A computer-controlled home-built shutter system blocks the IR laser in the pump arm between measurements (see Fig. 1.1). Taking back-to-back ground and excited state spectra significantly lowers the harmonic stability requirements; we require stability on the order of twice the exposure time ($\sim$ seconds), rather than the entire experimental run ($\sim$ hours).

Our spectrometer's CMOS camera has a bit depth of 16, corresponding to a maximum value of $2^{16} - 1 = 65,535$ counts before saturation. The exposure time is set so that the amplitude of the brightest harmonic on the detector is about 10% below this limit, which allows for an upward drift in harmonic yield to occur without invalidating the dataset. An exposure time of 3 seconds is typical for a 100 nm Ge sample at 125 Hz (375 laser shots).

Although the Spitfire laser system has a maximum repetition rate of 1 kHz, we perform solid state ATAS experiments at a much lower rate (125 or 250 Hz) by adjusting amplifier's Pockels cell firing rate. The lower repetition rate allows the sample to more fully relax between laser shots, reducing the effects of millisecond thermal processes on our measurements. It also reduces the average power on the sample for a given pulse energy, which lowers the steady state temperature of the sample. On the other hand, it allows us to increase the pulse energy while maintaining a constant average power on the sample.

During the experiment, the sample is rastered across the focus to reduce any deleterious effects of long term uninterrupted laser exposure. During motor movement, the IR beam is blocked with a shutter but the relatively weak XUV beam is allowed to remain on the sample. Each pair of measurements (ground state, excited state) in a given delay scan has a unique position on the sample. Typical step sizes are 200 μm, which is larger than

the measured XUV spot size of $\sim$12 μm and the IR spot size of $\sim$30 μm. Two raster schemes are schematically shown in Fig. 1.7. The method shown in the left panel produces a sawtooth pattern on the sample. This method gives very accurate positioning, as the vertical motor is almost always approaching the final position from the same direction. However, the diagonal steps are $\sqrt{N^2 + 1}$ times longer than the vertical steps, where N is the number of vertical steps in the pattern. As a result, there is a bimodal distribution of motor transit times between measurements. If the sample is not fully relaxed between motor movements, this will lead to an inconsistent measurement of the ground state $S_{gs}(E)$. The method shown in the right panel alleviates this problem by requiring equal step sizes. Measurements presented in this work were acquired using the method shown in the right panel.

Before measuring a sample's response for the first time, or after a major optical alignment, a map of the sample must be created. Creating this map serves two purposes: it verifies sample XUV absorption uniformity and it determines the motor coordinates of the sample's clear aperture. To avoid edge effects, the edges of the raster area are chosen to be 200 μm away from the edge of the clear aperture (see Fig. 1.7).

The data collection sequence can be summarized as *excited state → ground state → move motors*. Details of this sequence are as follows. First, the sample moves to a given raster position and delay wedge position, the IR shutter opens and an excited state measurement is taken. Then, the IR shutter closes and a ground state measurement is taken. Finally, the sample moves to the next raster position as the delay wedge pair moves to the next delay position. The system is programmed to wait for the wedges to become stationary before the next measurement begins.

Note that in this sequence, the time between the ith excited state and i^{th} ground state measurements is equal to the exposure time, but the time between the ith ground state measurement and the $(i+1)^{th}$ excited state measurement is equal to the delay wedge motor transit time[2]. This sequence is preferable to the alternative (*ground state → excited state →*

---

[2]In this analysis we neglect the role of the XUV-IR delay τ. However, $\tau \sim 1$ fs - 1 ps, which is neglible compared to the motor transit time ~ 1 s.

30 nm silicon nitride
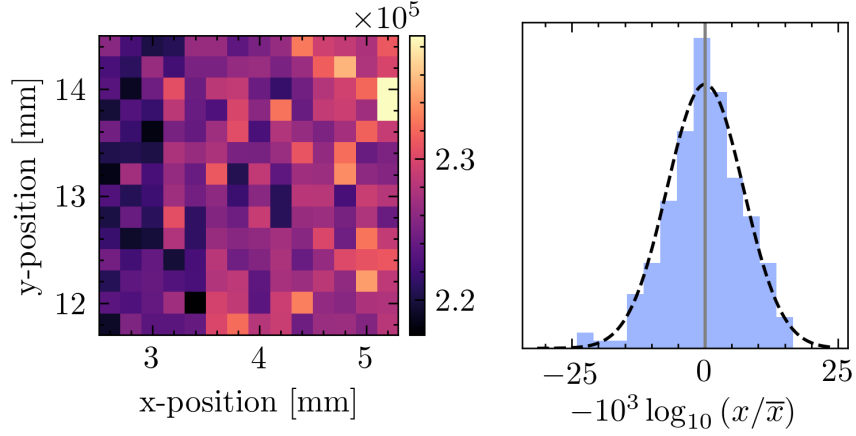
Figure 1.9: XUV transmission map of 30 nm silicone nitride freestanding membrane. Left panel: integrated harmonic peaks in the range ?? – ?? eV. Sample holder motor positions are indicated by x- and y-positions. Right panel: histrogram of logarithmic deviation of counts from the average.

move motors), as that would result in a delay step size-dependent relaxation time between the ith excited state and the $i+1^{th}$ ground state measurement. Since $\Delta A(E, \tau)$ is calculated between pairs of ground and excited state measurements at a given delay wedge position, the sequence *excited state* $\rightarrow$ *ground state* $\rightarrow$ *move motors* is preferred.

To further improve our signal to noise ratio, we average multiple delay scans together. A typical ΔA measurement will repeat a delay scan between 10 and 50 times. Each delay scan uses the raster points of the previous delay scan so there is a one-to-one mapping of delay to sample position.

damage thresholds, sample thickness, sample uniformity

creating XUV sample maps when we get a new. this allows us to map out the clear aperture of the sample, as well as checking the uniformity of the sample.

1.5 The Supporting Membrane

While most materials have an absorption edge within the range 25 - 150 eV, there are very few commercially available pre-fabricated materials with the requistite large clear aperture

plot of SiN transmission+error, compared to CXRO

Figure 1.10: top panel: raw XUV counts of no filter, Al filter, Al + SiN. bottom panel: measured transmission of Al filter, and of SiN membrane. also plotted are the CXRO transmission curves. the oscillations are artifacts of the measurement. details will follow in a later section.
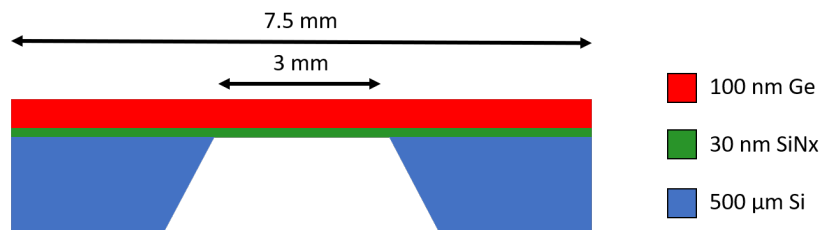
Figure 1.11: Cartoon showing the cross section of the free standing sample heterostructure. A 500 μm thick Si frame supports a freestanding 30 nm low stress silicon nitride membrane (Norcada QX7300X), upon which 100 nm of germanium has been deposited. The Si frame has a 3x3 mm^2 square clear aperture and a 7.5x7.5 mm^2 square external dimension. The taper of the Si frame thickness along the perimeter of the clear aperture forms a knife edge. In an ATAS experiment, the XUV and IR pulses propagate from the top to bottom of the figure.

and thickness. As shown in Fig. 1.7, most of the sample's area isn't directly used by the laser - it exists as a buffer between the grid of sample points.

An alternative to a single clear aperture is an array of micro-apertures, each with a diameter on the order of the IR spot size. The micro-apertures exist within a mechanically robust substrate and a thin membrane lies on top of the structure. This configuration significantly eases the material strength requirements by reducing the size of the unsupported area from cm-scale to sub-mm-scale. Fortunately, these arrays are commercially available from Silson, Norcada (silicon nitride membranes) and US Applied Diamond (diamond membranes), but we encountered technical difficulties in their implementation. Because the aperture size is on the order of the size of the IR focal spot, there is very little room for positioning error, and our motors were insufficiently precise for this application. Further, these arrays are typically only available in at most a 3×3 array, which provides an insufficient number of raster points for an experiment.

With these limitations in mind, we decided to use large aperture x-ray windows from Norcada. These windows consist of a mechanically robust Si frame substrate with a square clear aperture cut through the center. The structure is fabricated so that a thin membrane covers the clear aperture. A cross section is shown in Fig. 1.11.

Norcada offers these structures with either a silicon (polycrystalline or single-crystal) or a silicon nitride membrane. An ideal membrane is transparent to both XUV and IR wavelengths with a high damage threshold. Referring to Fig. 1.5, 100 nm of Si provides a relatively flat transmission curve from 25 to 100 eV. In constrast, 30 nm of silicon nitride has poor, but featureless, transmission at lower energies. Both materials transmit light below their bandgaps (5 eV for SiN and 1.14 eV for Si). Finally, silicon nitride's higher bandgap results in a significantly higher laser damage threshold [2, 3, 5]. Taking all these factors into account, we decided to use 30 nm silicon nitride membranes for germanium transient absorption experiments.

measurements of the nitride membrane: maps, histograms - showing how uniform it is. plot the transmission of the nitride membrane.

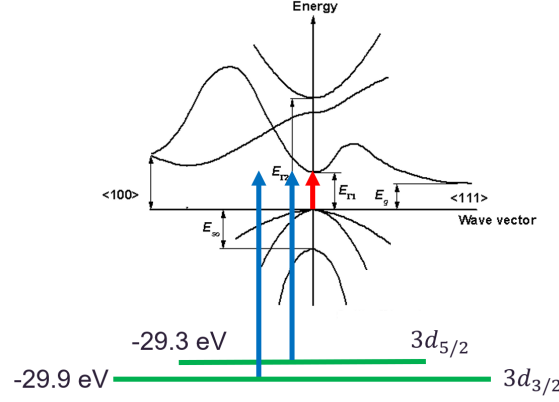On a similar note, experiments using WS_2 monolayer flakes were

Figure 1.12: Band structure and $3d$ states of Germanium. Blue arrows indicate XUV-induced transitions from the core levels to valence and conduction bands. Red arrows indicate IR-induced transitions across the band gap. Arrows are displaced horizontally for visual clarity. Figure adapted from [1].

Likewise, experiments with micro-flakes of WS_2 samples were attempted,

nano-particles and nano-flakes of TMDs – too difficult to index, too small for the IR focus (edge effects, and just smaller than the laser size), too inconsistent in thickness (double stacking is possible).

1.6 Germanium as a Sample

talk about the germanium sample, why it was chosen as a sample, how it was grown and how thick it was.

1.7 dialing in the IR parameters

IR power controlled by waveplate-polarizer pair and monitored during measurements using a photodiode (see Fig. 1.1). absolute measurements of the average power were taken with a power meter at the completion of the experiment. did intensity scans until the sample was destroyed, then backed off a little bit.

Ge-specific experimental parameters: wavelength, generation conditions, exposure time, MCP settings, rep rate, etc.

calculated excitation percentage, from lens calculations and measured IR power.

Ge IR absorption spectrum, and maybe band structure diagram

Figure 1.13: this figure shows the IR absorption of germanium from the literature. (citation). or maybe the n,k values from refractiveindex.info
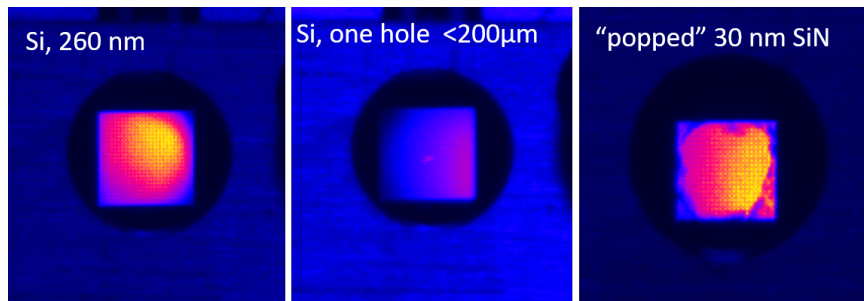

Figure 1.14: False color images showing laser drilled freestanding membranes. Left: pristine 260 nm thick Si membrane (Norcada). Middle: same sample, after a performing an IR power scan that exceeded the membrane's damage threshold. A <200 μm hole is visible as a cluster of bright pixels near the center of the membrane. Right: 30 nm SiN membrane after a similar power scan showing a "popped" membrane. Note the ragged edges near the clear aperture of the frame are all that remain of the membrane. The apparent brightness gradient across the samples is caused by inconsistent backlighting. Images were taken using the optical setup shown in the left panel of Fig. 1.8.
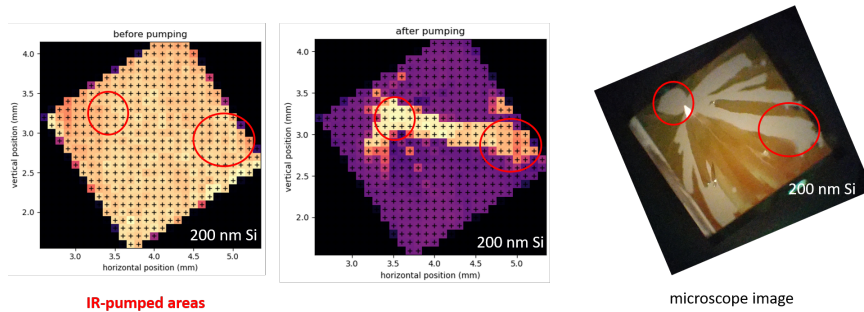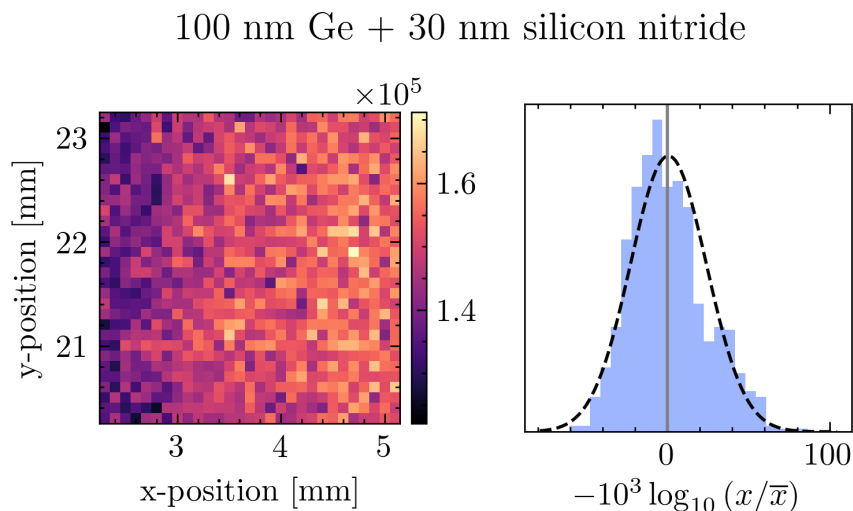

Figure 1.15: 200 nm silicon

Figure 1.16: Left panel: spatial mapping of integrated XUV counts **(integrated over what energy range?)** of a 100 nm Ge + 30 nm silicon nitride sample. Right panel: histogram of values from the left panel.

does the measured signal strength make sense? i.e., order of magnitude

show pictures of popped membranes. show delay spectrograms of drilled out samples.

1.8 50 nm Ge measurements

i think we have a dataset or two showing a weak signal.

1.9 100 nm Ge measurements

we went to 100 nm because the 50 nm was too weak.

1.10 Data Processing

The XUV photon spectrometer utilizes a flat field grating (Hitachi, 1200 l/mm) to spectrally disperse the XUV light. The grating is designed to focus along the spectral axis (horizontal direction) while preserving the spatial profile of the beam (vertical direction). The focus of the grating is incident on a 75 mm diameter imaging quality microchannel plate (MCP) array (Photonis), which converts the XUV photons into electrons via a nonlinear avalanche

data pipeline figure
- shows
PumpOn/Off
images, lineouts,
filtering, etc.

Figure 1.17: this figure shows the data processing pipeline. it shows how we start with PumpOn-Off 2D images and transform them into spectrograms. it includes steps like an absorbance (A) calculation, spectral lineouts, frequency filtering and smooth, energy calibration, etc.

top: pumpon &
pumpoff lineouts
bottom: delta-OD
calculation.

Figure 1.18: this figure shows, using real data, a pump off and pump on spectral lineout. in another panel, it shows the ΔA.

process with a gain of approximately $10^6 - 10^8$. These electrons strike a phosphor screen, which converts the electrons into visible photons (central wavelength ~ 480 nm). The visible photons exit the vacuum chamber via a glass feedthrough and are imaged by a lens and CMOS camera (Andor). The result is a two dimensional array of counts, with the horizontal axis representing the spectral content and the vertical axis representing the spatial profile of the beam.

talk about all the steps you use to process the data, starting from the 2d image and ending with the delta-A spectrogram.

mention calibration of spectrometer in passing, 2D image $\rightarrow$ 1D spectrum

Bibliography

[1] NSM Archive - Physical Properties of Semiconductors. http://www.ioffe.ru/SVA/NSM/Semicond/index.html.

[2] D. R. Austin, K. R. P. Kafka, Y. H. Lai, Z. Wang, C. I. Blaga, and E. A. Chowdhury. Femtosecond laser damage of germanium from near- to mid-infrared wavelengths. *Opt. Lett., OL*, 43(15):3702–3705, Aug. 2018.

[3] E. G. Gamaly, A. V. Rode, B. Luther-Davies, and V. T. Tikhonchuk. Ablation of solids by femtosecond lasers: Ablation mechanism and ablation thresholds for metals and dielectrics. *Physics of Plasmas*, 9(3):949–957, Feb. 2002.

[4] E. Gullikson. CXRO X-Ray Interactions With Matter. http://henke.lbl.gov/optical_constants/.

[5] L. Keldysh. Ionization in the Field of a Strong Electromagnetic Wave. *SOVIET PHYSICS JETP*, 20:1307–1314, May 1965.

[6] E. Nichelatti. Complex refractive index of a slab from reflectance and transmittance: Analytical solution. *J. Opt. A: Pure Appl. Opt.*, 4(4):400–403, July 2002.

[7] M. Schultze, K. Ramasesha, C. D. Pemmaraju, S. A. Sato, D. Whitmore, A. Gandman, J. S. Prell, L. J. Borja, D. Prendergast, K. Yabana, D. M. Neumark, and S. R. Leone. Attosecond band-gap dynamics in silicon. *Science*, 346(6215):1348–1352, Dec. 2014.